Journal of Structural Geology, Vol. 11, No. 1/2, pp. 37 to 50, 1989
Printed in Great Britain

0191-8141/89 $03.00 + 0.00
© 1989 Pergamon Press plc

From orientation to magnitudes in paleostress determinations using fault slip data

JACQUES ANGELIER

Tectonique Quantitative, Université Pierre et Marie Curie, 4 Place Jussieu, 75252 Paris Cédex 05, France

(*Received* 17 *December* 1987; *accepted* 2 *June* 1988)

Abstract—Determinations of reduced stress tensors using fault slip data yield the orientation of principal stress axes and the ratio Φ of the differences between principal stress magnitudes. The use of rupture and friction laws allows determination of the two remaining unknowns, that is, the reconstruction of the complete stress tensor. Taking into account the depth of overburden brings an additional constraint. The method is applied and discussed in the case of the Hoover Dam site (western U.S.A.), where large data sets and rock mechanics information are available. Differences between intact sample and rock mass properties account for apparent disagreements between paleostress levels determined in similar tectonic environments. Pore pressure plays an important role; where information about pore pressure is absent, zero and hydrostatic pore pressure cases should be considered as limits.

INTRODUCTION

FIELD studies have revealed that both major and minor faults commonly occur in the upper crust even in regions where deformation has remained very small (such as large basins and plateaus). The studies have also shown that qualitative and quantitative analyses of brittle structures provide a reliable key to understanding the distribution and evolution of paleostress fields through successive tectonic events. Thus, making detailed observations in available outcrops where faults are observed allows the reconstruction of some major characteristics of tectonism over a large area.

The additional information obtained from other structures such as tectonic joints (Hancock 1985), tension gashes and stylolites (Mattauer 1973) is also important, but will not be mentioned hereafter.

The first step in an investigation of faults consists of reconstructing the 'reduced stress tensor' in outcrops where populations of fault slip data have been collected. This particular tensor is, by definition, a linear function of the actual average stress tensor that has induced the fault slips. Because this linear function is chosen arbitrarily, the reduced stress tensor cannot yield the magnitudes of the principal stresses: σ_1 (maximum compressional stress), σ_2 (intermediate stress) and σ_3 (minimum stress). However, this reduced stress tensor contains valuable information: the order and orientation of the three principal stresses are the same as for the actual stress tensor and enable one to define the directions of compression and extension which prevailed during tectonic events. The magnitude of stress cannot be derived directly, because knowing the orientations and senses of shear stress on fault planes does not suffice to determine the complete stress tensor.

In the first section of this paper, the basic properties of the reduced stress tensor are summarized and its determination is briefly illustrated; methods are not discussed but are contained in Angelier (1984).

The aim of this paper is principally to propose a method of determining the complete stress tensor; that is, determining paleostress not only in terms of orientation but also in terms of magnitude, based primarily on fault slip data analysis. The method will be used to determine paleostress levels of Basin and Range late Cenozoic extensional tectonics at the Hoover Dam locality, Nevada–Arizona (Fig. 1).

THE REDUCED STRESS TENSOR: DETERMINATION AND UNKNOWNS

During the last 12 years, numerical methods have been proposed for reconstructing paleostress orientations using fault slip data. Underlying these methods is the stress–shear relationship described by Wallace (1951) and Bott (1959). Knowing the stress state, one determines the shear stress and hence the slip orientation expected on any plane. The first attempt at formulating and solving the inverse problem was published by Carey & Brunier (1974): knowing the slips and hence the shear stress orientations on various planes, one determines the average stress state. Subsequent methodological developments are those of Angelier (1975, 1979, 1984), Armijo & Cisternas (1978), Etchecopar *et al.* (1981), Angelier *et al.*(1982b), Gephart & Forsyth (1984) and Michael (1984).

Principal stress orientations and the stress ratio Φ: the methods

The basic assumption. In this paper, I consider the general case, where any planar discontinuity in a rock may be activated as a fault, regardless of its origin. The discontinuity may be either a pre-existing feature activated or reactivated (inherited fault) by the tectonic stress, or a fracture that develops during the tectonic event (neoformed fault).

The direct problem consists of determining the orien-

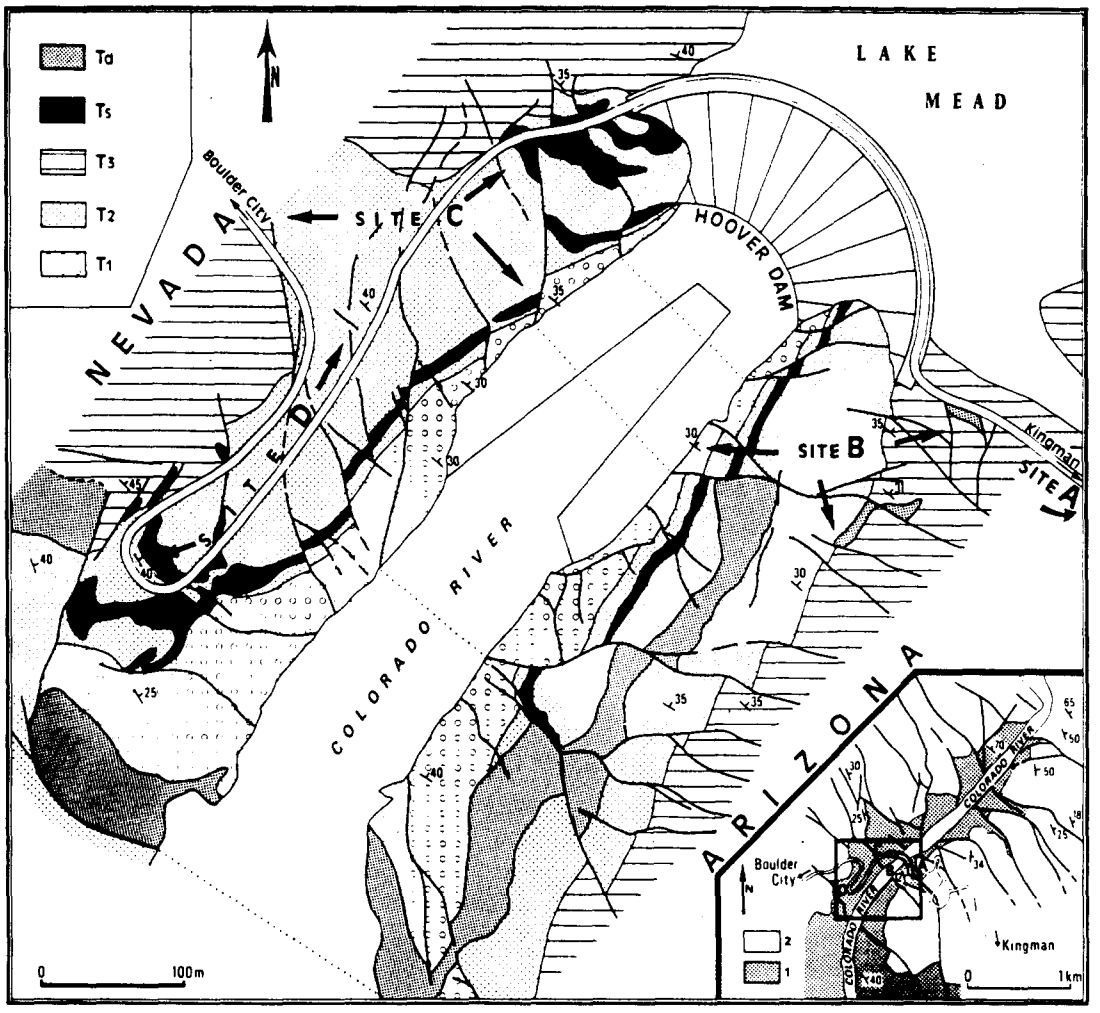

Fig. 1. Geological map of the Hoover Dam site, Nevada–Arizona (Angelier *et al.* 1985, after U.S. Bureau of Reclamation 1950 and written communication 1981). Faults, thick lines; stratal dips in degrees. T1, conglomerates; T2, lower welded ash-flow tuff; T3, upper welded ash-flow tuff plus volcanic breccia and basic latite flow; Ts, sill of latite; Td, dikes of andesite basalt. Fault slip data were collected in subsites A–B–C–D. Lower right corner: generalized map of the area (waters of Lake Mead removed) showing the pattern of faulted-tilted blocks (1, ash-flow tuffs and subjacent formations; 2, overlying lavas and sediments).

tation and sense of slip knowing the orientation of a fault plane, for a given stress tensor, **T**. The inverse problem consists of determining the mean stress tensor, **T**, knowing the orientations and senses of slip on numerous faults. In both cases, the basic assumption is that each fault slip (indicated by slickenside lineations) has the direction and sense of shear stress that corresponds to a single common stress tensor. However, data collection involves errors, dispersion occurs in local stress patterns and fault movements influence one another. In practice, one searches the best fit between all fault slip data that belong to a given tectonic event and a common unknown stress tensor.

The assumption that all faults which moved during the same tectonic event were moving independently but consistently with a single stress tensor is an obvious approximation; however, application to numerous actual cases has shown high levels of consistency as indicated by small values of average angles ($\mathbf{s}, \tau$). Note that ($\mathbf{s}, \tau$) is the angle between the observed slickenside lineation or slip vector, **s**, and the theoretical shear stress vector, τ, shown in Fig. 2 and derived from the stress tensor solution of the problem.

The Hoover Dam case. Figures 3 and 4 summarize some of the results obtained in the Hoover Dam site, 40 km southeast of Las Vegas, Nevada, where deep downcutting by the Colorado River and excavations related to dam construction have provided fresh outcrops in faulted and tilted Miocene rocks (Fig. 1). A large number of fault slip data could be collected, so that the tectonic history can be reconstructed accurately. A description, including discussion of the regional geological setting (Longwell 1936, Anderson 1969, 1971, 1973), is found in Angelier *et al.* 1985 (Fig. 1). To summarize, two major stages of the late Cenozoic tectonic evolution at the Hoover Dam site have been distinguished. The first stage consists of dip-slip and strike-slip faulting, with associated stratal tilting that affects fault blocks, in agreement with a N50°E direction of extension. The second stage mostly consists of post-tilt dip-slip, oblique-slip and strike-slip faulting, with a dominant N105°E direction of extension.

In more detail, four substages can be distinguished in the Hoover Dam site. The first two substages correspond to the same direction of extension N50°E, and they are separated on a geometrical basis as mainly-pre-tilt and

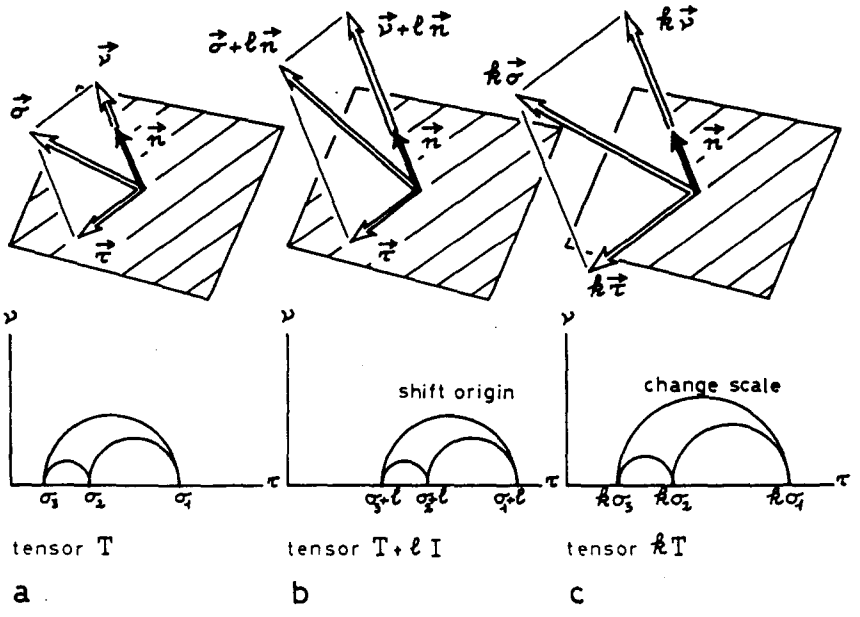

Fig. 2. The two unknowns of the reduced stress tensor. Column a: the stress tensor **T** with principal stress magnitudes σ_1, σ_2, σ_3 (see Mohr circles) induces a stress vector $\boldsymbol{\sigma}$ on the fault plane with unit normal vector, **n**. The stress vector $\boldsymbol{\sigma}$ may be split into normal stress, ν, and shear stress, τ. Column b: adding any isotropic stress tensor, $l\mathbf{I}$ (l is any real number, **I** is unit matrix) changes **T** into $\mathbf{T} + l\mathbf{T}$, adds l to each principal stress (shifts Mohr circles), changes $\boldsymbol{\sigma}$ into $\boldsymbol{\sigma} + l\mathbf{n}$, and ν into $\nu + l$n; shear stress, τ, remains unchanged. Column c: multiplying the stress tensor **T** by any positive real number, k, changes scale of Mohr circles by factor k and multiplies all components of stress by same factor, k, so that neither orientation nor sense of shear stress τ vary.

post-tilt, respectively (Fig. 4). Each substage includes two paleostress states, one with predominantly dip-slip normal faulting and the other with predominantly strike-slip faulting. These first two substages are grouped in a single tectonic event (the first stage) which induced extensive block faulting and tilting. Qualitative evaluations of fault slip chronology (Fig. 5) indicate that during each substage, dip-slip and strike-slip faulting probably alternated in time. The last two substages (the second stage) correspond to post-tilt tectonic activity solely, with a direction of extension rotating clockwise from N80°E to N105°E. Again, each substage includes probable oscillations in time between dip-slip and strike-slip faulting (as shown by complexly intricate successions of dip-slip and strike-slip movements).

Finally, the paleostress history revealed by fault slip data analysed at Hoover Dam site includes four pairs of main stress states, each pair corresponding to a substage. I define four pairs rather than eight individual stress states, because for each pair the minimum stress axis, σ_3, is stable while the other two other axes interchange. These pairs are called n_i and d_i, where n and d denote predominantly normal dip-slip and strike-slip modes, respectively, and numbers, i, indicate succession from 1, older, to 4, younger (Table 1). Pairs 2 and 4 are shown in Fig. 3. For each pair n_i, d_i, determinations of stress tensors allow a reliable separation of two types of stress: one type corresponds to predominant normal dip-slip faulting (n_i), the other type, with σ_2 close to vertical, corresponds to predominant strike-slip faulting (d_i). However, the common orientation of extension (compare n and d for each pair in Table 1) and the complex and intricate fault slip relative chronologies suggest that these two types of stress alternated in time within each tectonic substage. During the first tectonic event, block tilting occurred with N50°E extension ($n_1 - d_1$ and

Table 1. Results of paleostress tensor determinations

Fault set	Number of fault slip data	Sum of weights	Axis σ_1 trend plunge	Axis σ_2 trend plunge	Axis σ_3 trend plunge	Ratio Φ	Average angle s, τ	Column in Fig. 3
n_1	112 (102)	152	244 62	149 03	057 28	0.21	11	—
n_2	158 (150)	239	269 84	139 04	049 04	0.22	15	a
n_3	132 (126)	204	199 89	348 01	078 01	0.18	9	—
n_4	115 (105)	151	212 86	019 04	109 01	0.30	16	c
d_1	120 (111)	150	147 00	241 87	057 03	0.12	8	—
d_2	131 (130)	162	148 00	240 81	058 09	0.27	11	b
d_3	178 (167)	249	170 02	278 85	080 05	0.18	8	—
d_4	127 (125)	197	189 01	319 89	099 01	0.33	10	d

$n_1 - n_4$, predominantly normal fault sets; $d_1 - d_4$, predominantly strike-slip fault sets. Numbers in parentheses refer to fault slip data including sense of motion. Weights depend on fault size and offset. All angles in degrees. σ_1, σ_2, σ_3, Φ and (s, τ) defined in text. Fault slip data sets n_2, d_2 and n_4, d_4, illustrated in Fig. 3.

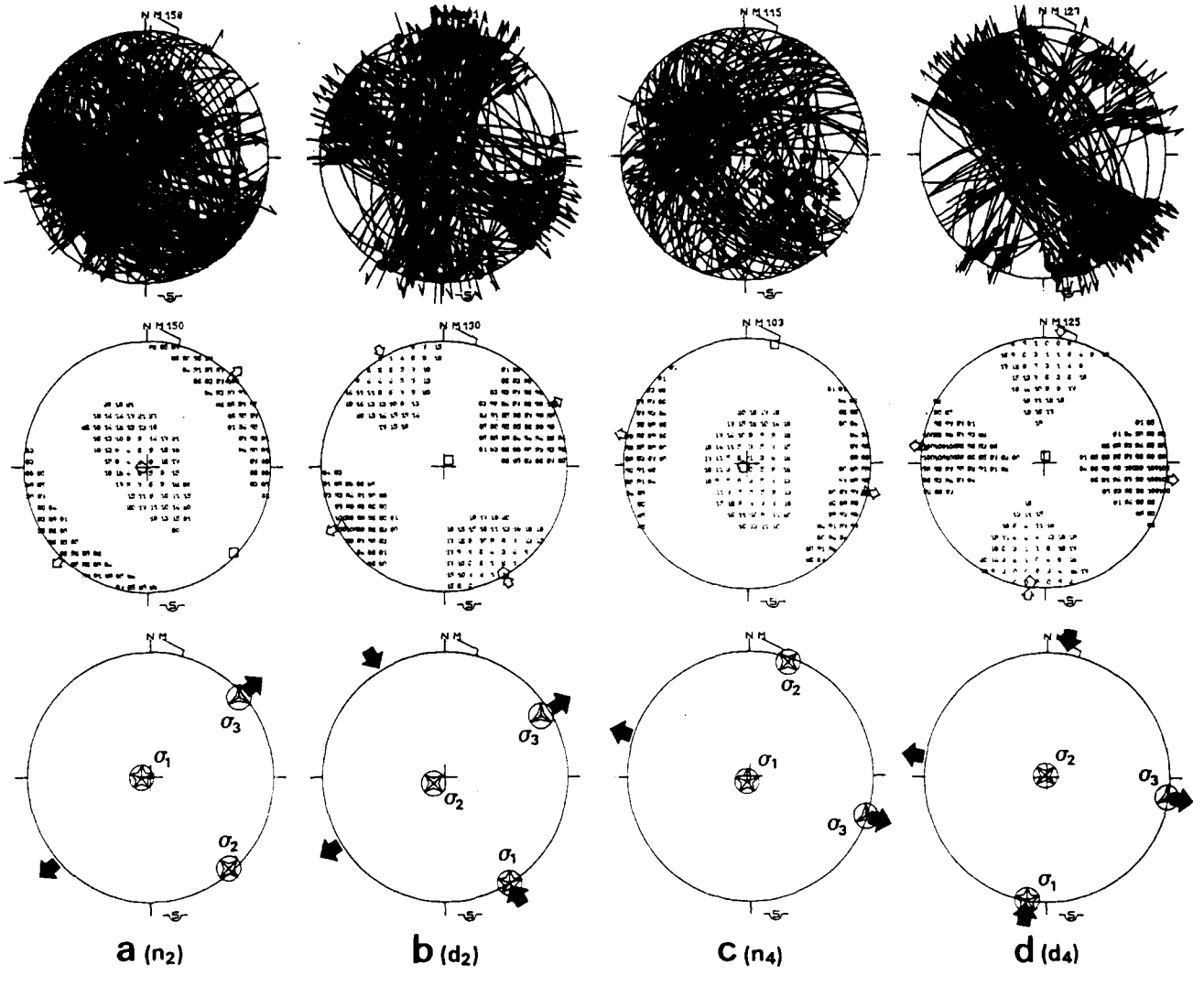

Fig. 3. Examples of fault slip data sets and determination of the reduced stress tensor. Hoover Dam site, Nevada–Arizona. All diagrams are Schmidt's projections, lower hemisphere. Columns (a), (b), (c) and (d) correspond to different subsets (n_2, d_2, n_4 and d_4, from older to younger; see text). Upper row: projection of fault planes, with slickenside lineations as dots with arrows (outward for normal motion, double for strike-slip motion). Middle row: application of the P- and T-dihedra method; small percentages indicate high compatibility for compression (e.g. 3 means that 3% of faults do not fit compression along corresponding orientation), high percentages indicate high compatibility for tension (e.g. 97 means that 97% of faults fit with tension). Preferred axes of consistency regions added as small open symbols. Lower row: results of determination of reduced paleostress tensors; principal stress axes σ_1, σ_2, σ_3 are shown as circled 5-, 4- and 3-branch stars, respectively; wide black arrows indicate directions of extension (divergent) or compression (convergent). Additional information (e.g. Φ ratio) given in Table 1.

$n_2 - d_2$ substages); during the second tectonic event, the direction of extension changed clockwise from N80°E to N105°E ($n_3 - d_3$ and $n_4 - d_4$ substages).

Paleostress axes and ratio Φ

Figure 3 illustrates the determination of stress orientations including fault slip data for substages n_2-d_2 and $n_4 - d_4$ of the Hoover Dam site, including data plot, use of P- and T-dihedra method and computation of reduced paleostress tensor (from top to bottom in Fig. 3). Plotting the collected fault slip data in the diagrams of the upper row only aims at illustrating the variety of fault orientations: stereographic projection of fault planes and slickenside lineations results in diagrams which look like balls of string. Conjugate fault patterns have been found and provide a simpler key to decipher complex fault slip distributions (Fig. 4).

Stress axes are shown in the lower row of diagrams of Fig. 3. The methods have been discussed in detail in an earlier paper where the function adopted in a least-squares minimization procedure is referred to as S_3 (Angelier 1984). This function decreases with the angle (s, τ) already defined and is minimum when the slip vector s has the same orientation and sense as the shear stress vector τ. Figure 3 and Table 1 show that for each substage, normal and strike-slip faulting modes are related through permutations between principal stresses σ_1 and σ_2. Table 1 contains the major parameters of the determinations made with the eight subsets.

In addition to the orientation of each principal stress axis (σ_1, maximum compressive stress; σ_2, intermediate

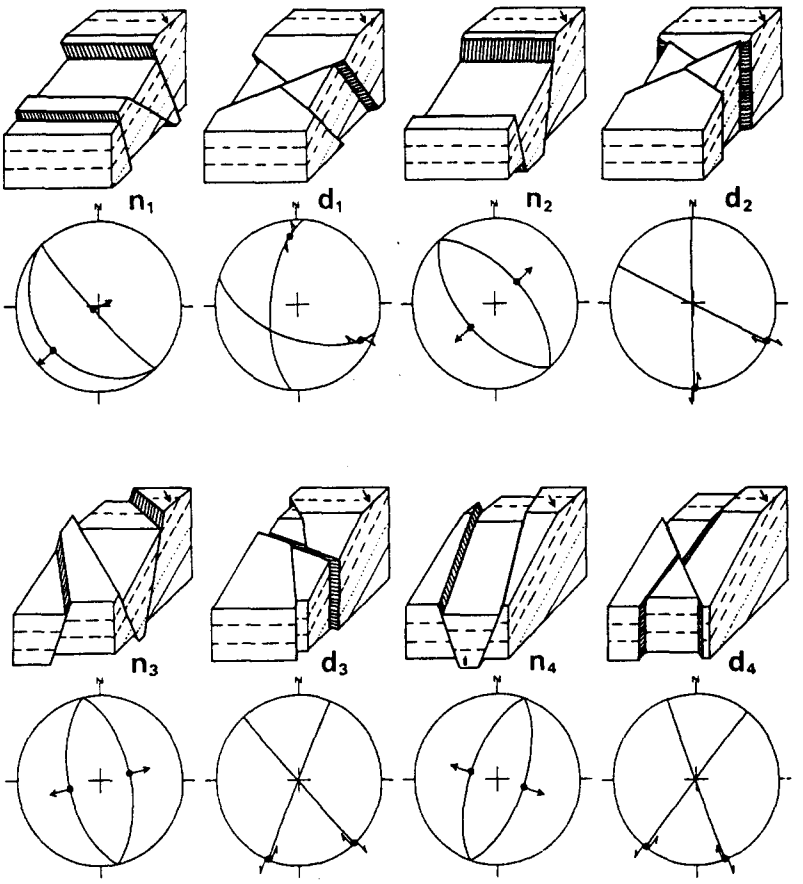

Fig. 4. Conjugate fault sets identified at Hoover Dam (schematic), with corresponding diagrams (Schmidt projection of fault planes and slickenside lineations, lower hemisphere, as in Fig. 3). Present attitude shown by a small arrow on top of faulted block which indicates north. Arrangement of conjugate sets relative to tilted bedding reflects faulting–tilting chronology. n_1 and d_1, N55°E extension: pre-tilt normal and strike-slip faults (respectively). n_2 and d_2, n_3 and d_3, n_4 and d_4: post-tilt normal and strike-slip faults related to N55°E, N80°E and N105°E trends of extension, respectively. Compare n_2, d_2, n_4 and d_4 with corresponding diagrams of Fig. 1.

stress; σ_3, minimum stress), the computation of the stress tensor enables one to determine a relationship between the magnitudes of the three principal stresses. This relationship is conveniently expressed by a 'ratio of principal stress differences', Φ, which may have values from 0 to 1:

$$\Phi = \frac{\sigma_2 - \sigma_3}{\sigma_1 - \sigma_3}.$$

This ratio has been defined as ϕ by Angelier (1975). The lower case symbol used first has been changed into a capital Φ, due to possible confusion with the angle of friction in the Coulomb–Mohr equation, commonly called ϕ (e.g. Jaeger 1969). A different definition of the ratio of principal stress differences was used implicitly by Bott (1959), and explicitly by Armijo & Cisternas (1978) who employed the symbol R

$$R = \frac{\sigma_z - \sigma_x}{\sigma_y - \sigma_x}.$$

The difference between Φ and R lies in the range of possible values. Whereas Φ may vary from 0 to 1 (because $\sigma_1 \geq \sigma_2 \geq \sigma_3$), R may have values from $-\infty$ to $+\infty$ (because principal stress magnitudes σ_x, σ_y, σ_z are considered without any assumption about their order). Three different values of R (e.g. 2, 0.5 and -1) may consequently correspond to a single value of Φ (in this case, 0.5). The significance of the symbol Φ has remained unchanged (e.g. Michael 1984). In contrast, the symbol R has been sometimes used either with the same significance as Φ (Etchecopar *et al.* 1981) or even with new and different definitions (Lisle 1979, Gephart & Forsyth 1984), thus generating some confusion. I consequently suggest adoption of unambiguous symbols: Φ (Angelier 1975) or R (with its earliest definition by Armijo & Cisternas, 1978).

Extreme values of Φ correspond to stress ellipsoids of

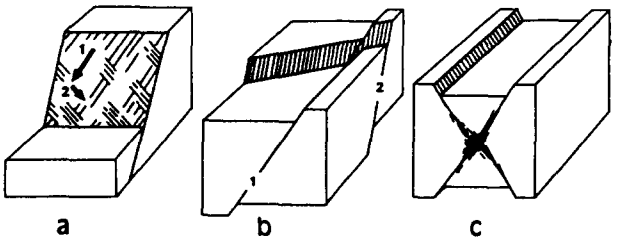

Fig. 5. Individual evaluation of relative chronology of faulting. (a) Successive fault slips 1 and 2. (b) Older fault, 1, offset by younger fault, 2. (c) Synchronous fault slips. Note than in (a) and (b) successive motions may belong to a single event. See also Fig. 4 (chronology of conjugate faulting and tilting).

revolution (two principal stresses magnitudes are equal), with $\sigma_2 = \sigma_3$ ($\Phi = 0$) or $\sigma_2 = \sigma_1$ ($\Phi = 1$). Other values correspond to actual triaxial stress ($\sigma_1 > \sigma_2 > \sigma_3$). As Table 1 shows, values of Φ computed at the Hoover Dam site are consistent and average 0.2, regardless of tectonic type (predominantly dip-slip or strike-slip) or stage (older to younger).

Finally, taking into account the number of data and the sources of dispersion, the average angles (s, τ) are small and reveal a high level of consistency within each set (11° on average: Table 1).

Significance and limits of the methods

Simple graphical methods. Firstly, the geometrical analysis of conjugate fault systems (Fig. 4) allows determination of the orientation of principal stress axes in a very simple way, based on the search for symmetries and taking into account shear senses (Anderson 1942). Slickenside lineations are perpendicular to the intersection of fault planes (Fig. 4) and σ_1 and σ_3 axes bisect the acute and obtuse angles between faults. Conjugate faults are neoformed; that is, fault surfaces do not exist prior to the tectonic event and develop as shear fractures induced by stress. This method has obvious limitations: the presence and the identification of neoformed conjugate faults are required, and oblique faults cannot be taken into account. In addition, the analysis of conjugate fault systems cannot yield the value of Φ, which is controlled by faults oblique to stress axes (because modifying the value Φ does not affect shear stress orientation on a plane that contains any principal stress axis).

Secondly, the P- and T-dihedra method (Angelier & Mechler 1977) enables one to easily constrain the orientation of stress axes for a population of faults of any kind (neoformed or inherited). Confidence areas for σ_1 and σ_3 axes are thus obtained on the sphere (Fig. 3). However, some information contained in the fault slip population is lost (especially, the uniqueness of the ratio Φ and the distinction between fault plane and auxiliary plane). As a result, this robust method, with benefits of directness and ease of visualization, cannot provide the most complete and accurate results. Note, however, that because there is no need to distinguish fault plane and auxiliary plane, the P- and T-dihedra method is directly applicable to focal mechanisms of earthquakes (see Angelier & Mechler 1977). Lisle (1987) suggests how the P- and T-dihedra method can be made more efficient as a search procedure for the principal stresses.

Numerical computations. Thirdly, the numerical computation of a stress tensor is the ultimate step for monophase fault populations (i.e. faults moving within a single tectonic event with homogeneous stress). It involves the minimization of a function that decreases with individual angles between shear stress and slip vector, thus giving the reduced stress tensor (as defined earlier). Various procedures and functions have been described and discussed (Angelier 1984). For focal mechanisms of earthquakes, it is necessary to identify the fault plane and the auxiliary plane among nodal planes, except if the Φ ratio is close to 0 or 1 (in these particular cases, slip on any nodal plane, perpendicular to the other nodal plane, is consistent with a single stress tensor: see Angelier 1984).

In addition, where data sets are heterogeneous and polyphase (i.e. mixed fault slips belonging to two or more tectonic events) more complex methods involve heavier search processes in order to separate automatically data classes and related stress tensors that correspond to successive paleostress states. In the Hoover Dam case, the separation of successive tectonic substages was undertaken using more than 40 individual cases of relative chronology (successive fault slips or fault intersections as in Fig. 5). Because successive fault motions may belong to a single paleostress state, careful compilation of these observations was done. The relationship to bedding attitude was taken into account (pre-tilt and syn-tilt faulting, Fig. 4). Finally, iterative clustering analysis resulted in a complete separation of subsets in terms of mechanical consistency (Angelier *et al.* 1985): the results were found to be consistent with the qualitative individual evaluations made first.

Interest and limits of the methods. All these methods aim at identifying paleostress states. Computing deformation related to fault tectonics requires collection of offset data (the amount of displacement) in addition to orientation data (the direction and sense of fault slip). Particular methods have been proposed (Gauthier & Angelier 1985).

Paleostress states are reconstructed at various scales; one may collect slip data on minor or major faults, in small sites or over large areas. In the Hoover Dam case (Fig. 1), all data were collected in a small area (less than 1km^2) and faults have offsets ranging from 1 cm to tens of metres. Special attention was paid to the comparison between major and minor fault sets in terms of geometry and paleostress determinations. Results did not differ significantly between fault sets, showing that at Hoover Dam, as in many other sites, minor fault patterns reflect tectonics on a larger scale (Angelier *et al.* 1985).

To interpret results of paleostress analyses at the regional scale, it is necessary to compare paleostress reconstructions from numerous sites. A map of stress trajectories is thus drawn for a given tectonic event. Examples of such regional analyses include geodynamic implications for collision zones (Taiwan: Barrier & Angelier 1986), continental platforms (Western Europe: Bergerat 1987) and regions of widespread extensional tectonism (Aegean: Angelier *et al.* 1982a).

Local heterogeneity of stress near faults is neglected in a paleostress reconstruction. Large-scale deviations of stress trajectories in the vicinity of major fault zones can be reconstructed provided that numerous sites of fault slip data collection are available in the area. It is important to bear in mind that paleostress orientations are reconstructed in the present reference system and that block rotations may have occurred during or after the tectonic event considered (such problems have been

mentioned in the Hoover Dam paper, Angelier *et al.* 1985). Other limitations of the methods have been discussed already (Angelier 1984).

Obvious traps include landslide phenomena and local variations of stress patterns (such as normal faults related to thrusts, or reverse faults in extensional tectonic environments); such effects should not be attributed to independent tectonic events.

Permutations of stress axes σ_1 and σ_2 or σ_2 and σ_3 commonly occur during tectonic events, the most frequent switches being σ_1/σ_2 for extensional tectonics and σ_2/σ_3 for compressional tectonics. The results shown in Table 1 and Fig. 3 illustrate such changes from predominantly normal to predominantly strike-slip faulting modes (σ_1/σ_2 permutation), for a single substage of extensional fault tectonics. Such permutations induce apparent complexity, with several paleostress patterns for a single tectonic event. Rotations also result in increasing complexity of fault slip distributions and in apparent complexity of paleostress evolution, such as in the Hoover Dam case where tilt occurs during the first tectonic stage (Fig. 4).

Finally, one must carefully distinguish between individual paleostress state (characterized by constant orientation of stress axes and constant ratio Φ), independent tectonic event (characterized by constant orientation of stress axes with possible variations of stress magnitudes and of ratio Φ) and major tectonic phase. The latter is characterized by a dominant tectonic mode, extensional or compressional, that prevailed during a significant time span, with possible changes in orientations of stress axes and magnitudes of stresses. In the case of the Hoover Dam, it has been possible to distinguish eight paleostress states (Table 1) which correspond to two main tectonic events in the late Cenozoic evolution of the Basin and Range (Zoback *et al.* 1981).

From the reduced stress tensor to the complete stress tensor

The complete stress tensor contains six independent variables: three variables indicate the orientation of the three orthogonal principal axes; the three remaining values describe the magnitudes of the principal stresses σ_1, σ_2 and σ_3. As Fig. 2 shows, adding any isotropic stress of magnitude 1, or multiplying by a positive scale factor k, obviously affects the magnitude of the stress tensor and respectively results in shift or size variation of the Mohr circle. However, it does not change the orientation of the principal stress and cannot modify the orientation and sense of shear stress on any plane. As a consequence, if **T** is the stress tensor calculated from fault slip data, any stress tensor $k\mathbf{T} + l\mathbf{I}$ will equally fit the data (Fig. 2).

In turn, one has no access to the values of k and l in that only fault slip orientations and senses are used to determine the stress. Only four variables of the stress tensor can be obtained: the orientations of the three principal axes and the ratio Φ. This implies that in order to solve the inverse problem it is convenient to adopt a particular form of the stress tensor. This form contains four variables (the unknowns of the problem) with an arbitrary choice of k and l; it is the 'reduced stress tensor'. Two types of reduced stress tensors, suitable for analytical and numerical minimization procedures respectively, have been presented elsewhere (Angelier 1984).

To reconstruct the complete stress tensor, one must compute two values (corresponding to k and l) after having determined a reduced stress tensor. The position and the size of the Mohr circles are thus fixed (Fig. 2). This new step will be discussed in the next section.

DETERMINATION OF PRINCIPAL STRESS MAGNITUDES

Three different criteria may be used in order to determine the two variables that have been left unknown in the reduced stress tensor. These three criteria are illustrated schematically in Fig. 6 and will be discussed in more detail in the case of the Hoover Dam site.

Rupture, friction and depth: three criteria, two variables

Constraints from failure envelope. Firstly, a typical failure envelope is shown in the Mohr diagram (shear stress vs normal stress) of Fig. 6 (a). The existence of neoformed conjugate faults can be easily detected within the fault slip data set according to their geometrical properties (Anderson 1942). By definition, the normal and shear stress magnitudes for conjugate faults correspond to a point on the largest Mohr circle, and the characteristic dihedral angle 2θ between these faults is

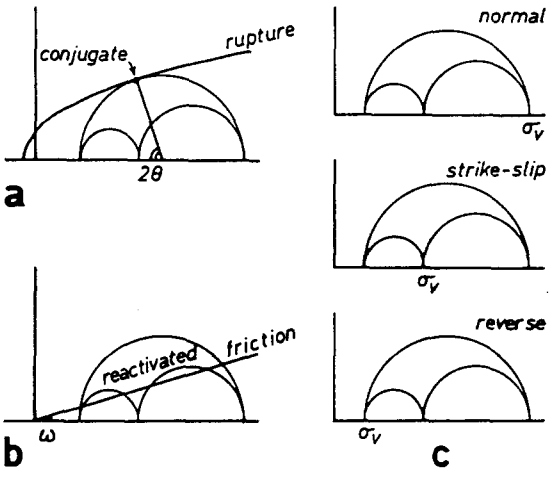

Fig. 6. Three criteria to determine the magnitudes of the principal stresses knowing orientations of stress axes and stress ratio Φ. Mohr diagrams (shear stress as ordinates, normal stress as abscissae). (a) Neoformed conjugate faults, with characteristic angle 2θ, define a point where largest Mohr circle ($\sigma_1 - \sigma_3$) should be tangent to failure envelope. (b) Inherited faults resulting from reactivation of older faults (or activation of older rock discontinuities as faults) correspond to points between the three Mohr circles; these points should be above friction line characterized by angle ω, thus fixing ratio Ψ between maximum and minimum stresses (see text). (c) Knowing paleo-depth during the tectonic event, hence lithostatic pressure, fixes the magnitude of vertical principal paleostress σ_v (σ_1, σ_2, or σ_3 depending on type of fault tectonics).

easily read in the diagram. Because such faults are neoformed (i.e. develop during the tectonic event considered), the largest Mohr circle should be tangent to the failure envelope at the corresponding point (Fig. 6). Determination of paleostress in southern Germany, based on analyses of conjugate strike-slip faults and rock mechanics experiments, have been carried out by Bergerat *et al.* (1982, 1985).

In theory, the geometrical relationship shown in Fig. 6 (a) between a Mohr circle and a failure curve should be sufficient to completely determine the magnitudes of extreme principal stresses, σ_1 and σ_3, because the failure envelope is non-linear so that the knowledge of the angle 2θ constrains the slope of the rupture curve at the point of tangency. This is not true in practice, because the slope of the failure curve varies little (much of the envelope is rather straight), except for low values of normal stress. As a result, in general, knowing the angle 2θ simply enables one to check the compatibility between this conjugate system angle and the average slope of the failure envelope, within a certain range of normal stress values.

To summarize, using the geometrical relationship shown in Fig. 6 (a), one can reliably determine one relationship between extreme principal stress magnitudes σ_1 and σ_3, provided that neoformed conjugate faults are found and the rupture law of the rock mass is known. Because the failure envelope is not a straight line, this relationship is non-linear: the average magnitude $(\sigma_1 + \sigma_3)/2$, that is the abscissa of the centre of the main Mohr circle, increases more rapidly than the difference $(\sigma_1 - \sigma_3)/2$, that is the radius of this circle. Another relationship is still necessary to determine σ_1 and σ_3.

Constraints from friction line. Secondly, a typical initial friction curve is shown in the Mohr diagram of Fig. 6 (b). According to physical experiments, the law is considered linear and no initial resistance to slip is assumed, so that this curve is a straight line intersecting the origin (Fig. 6b). This initial friction law is characterized either by the angle ω or by the corresponding slope called μ. All inherited faults correspond to pre-existing rock discontinuities (e.g. bedding planes, joints, older faults and fractures) which may slip under the stress considered. The occurrence of slip on such discontinuities is controlled by friction laws (Jaeger 1969), so that the corresponding points in the Mohr diagram (these points lie by definition on or between the three Mohr circles) should be found on or above the initial friction curve (and, of course, beneath the failure curve and the maximum friction line). Friction laws have been applied to the fault patterns of north central Nevada by Zoback & Zoback (1980) to constrain the ratio between extreme principal stresses and to determine the strength of the crust.

In the Mohr diagram (shear stress vs normal stress), if the initial friction law is known, all points that represent fault slips should lie above the corresponding friction line shown in Fig. 6 (b); otherwise, slip would not occur. This requirement obviously imposes a constraint on the size of the Mohr circle. If the slope of the friction line is unknown, it can be found provided that inherited faults are numerous enough to define the lower boundary of the mass of related points in the Mohr diagram. In both cases, considering friction laws assigns geometrical constraints on the Mohr circles. A second relationship between extreme principal magnitudes is thus obtained. This relationship is linear and conveniently expressed by a ratio that will be referred to as Ψ:

$$\Psi = \frac{\sigma_3}{\sigma_1}.$$

The ratio between the radius $(\sigma_1 - \sigma_3)/2$ of the largest Mohr circle and the abscissa $(\sigma_1 + \sigma_3)/2$ of its centre is thus fixed:

$$\frac{\sigma_1 - \sigma_3}{\sigma_1 + \sigma_3} = \frac{1 - \Psi}{1 + \Psi}.$$

Combining rupture and friction laws. Finally, the two geometrical constraints shown in Figs. 6 (a) & (b) fix the magnitudes of extreme principal stresses, σ_1 and σ_3, provided that the mechanical properties of the rock mass in terms of rupture and friction laws are known (shear stress vs normal stress).

Because the ratio Φ of the differences between the three principal stresses has already been determined while computing the reduced stress tensor (Fig. 3 and Table 1), the magnitude of intermediate principal stress, σ_2, is immediately obtained. Inherited faults, especially faults oblique to all stress axes, play a major role in the determination of stress magnitudes. First, they provide the only way to determine the value of the stress ratio Φ in a significant way while reconstructing the reduced stress. Second, they bring constraints in terms of initial friction (points in the Mohr diagram lie at the intersection between Mohr circles and abscissa axis for planes perpendicular to one stress axis; they lie along Mohr circles for planes containing one stress axis; they are found between the three Mohr circles for planes oblique to all axes).

The vertical stress. Determining the lithostatic load gives the value of the vertical stress, σ_v. Practical analyses show, and theoretical reasoning suggests, that one of the principal stress axes is generally vertical during a tectonic event (rotations may occur later). Depending on the rank (σ_1, σ_2 or σ_3) of this principal stress axis, predominantly normal, strike-slip or reverse faulting modes (respectively) develop (Fig. 6c). Provided that the depth at the time of the tectonic event considered can be determined as well as the average density of overlying rocks, one thus obtains additional information (the value of one principal stress). Erosional exhumation or sedimentary burial must be taken into account carefully. This reasoning has been used by many authors.

Actual values. To conclude, in sites where the reduced stress tensor has been determined, rock mechanics con-

siderations enable one to determine three independent relationships between the magnitudes of σ_1 and σ_3 (Fig. 6). Therefore, not only the two remaining unknowns of the stress tensor are firmly constrained, but also possible discrepancies between rupture, friction and depth data are detected. In sites where rupture, friction or depth data are absent, the information can be inferred from this analysis but cannot be checked. For instance, determination of principal stress magnitudes using the rupture and friction rock mechanics criteria shown in Figs. 6 (a) & (b) implicitly assigns a certain value to the depth of overburden, the likelihood of which should at least be discussed.

Typical rupture and friction laws are found in the rock mechanics literature (e.g. Jaeger & Cook 1969, Byerlee 1978). A compilation of published rock mechanics analyses, not discussed herein, has resulted in selecting empirical relationships rather than theoretical laws: Hoek & Brown (1980) and Hoek & Bray (1981) have presented a failure criterion that satisfactorily accounts for the results of experiments and corresponds to the following equation:

$$\frac{\tau}{\sigma_c} = A\left(\frac{\sigma}{\sigma_c} - T\right)^B,$$

where τ is the shear strength, σ the normal stress and σ_c the uniaxial compressive strength of intact rock. A, B and T are constants defining the shape of the Mohr failure envelope. This empirical relationship has been applied to intact as well as closely jointed rock masses, and tables of empirical constants A, B and T have been published for various lithologies and various degrees of rock mass quality (Hoek & Bray 1981). Figure 7 (a) illustrates corresponding failure curves for volcanic rocks such as andesite, dolerite, diabase and rhyolite, with rock mass quality decreasing from intact rock (curve A) to rock with closely spaced and heavily weathered joints (curve F).

Figure 7 (b) shows the initial friction and maximum friction laws that have been proposed by Byerlee (1978), based on a compilation of experimental results. Byerlee has shown that whereas at low normal stress (up to 5 MPa) the shear stress required for sliding depends on surface roughness, at higher normal stress this effect is diminished and friction is nearly independent of rock type. In the shear stress–normal stress diagram, most points corresponding to friction at normal stresses up to 600 MPa plot in the stippled area between the two lines shown in Fig. 7 (b). The lower boundary (initial friction) corresponds to a minimum slope of about 0.3, while the upper boundary (maximum friction) corresponds to slopes of about 0.85 and 0.5 (below and above 200 MPa, respectively). The most interesting property of these experimental relationships between normal and shear stresses is their linear character. Amplitudes of minimum shear stress, τ, and normal stress, σ, during sliding are closely approximated by a linear law:

$$\tau = \mu\sigma.$$

One may observe in Fig. 7 that for a rock mass of poor

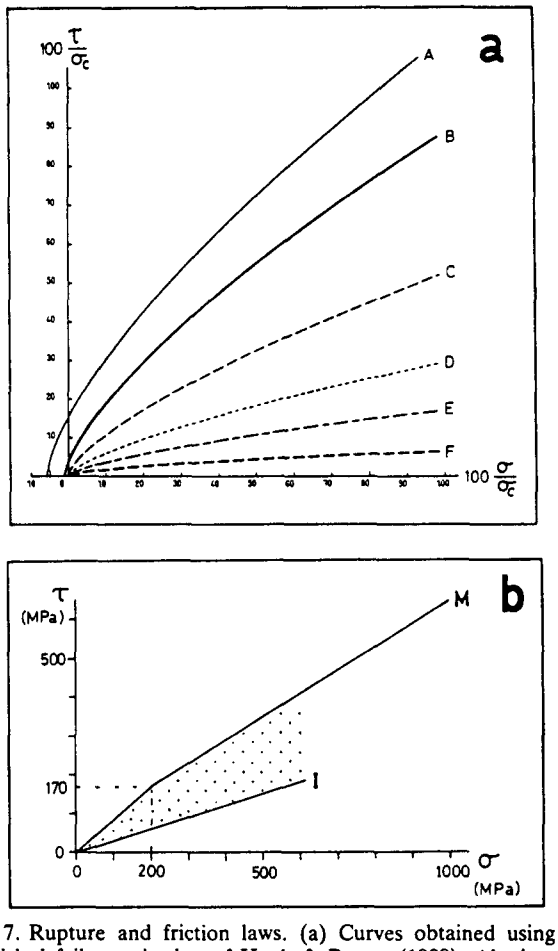

Fig. 7. Rupture and friction laws. (a) Curves obtained using the empirical failure criterion of Hoek & Brown (1980). Abscissa and ordinate: dimensionless normal stress, σ, and shear stress, τ, respectively (σ_c, compressive strength). Curves A–F refer to decreasing rock mass quality (A intact rock pieces; F heavily jointed and weathered rock mass). Curves plotted according to parameters tabulated by Hoek & Bray (1981) for igneous fine-grained rocks. (b) Initial friction (I) and maximum friction (M) curves (adapted from Byerlee 1978). Normal stress, σ, and shear stress τ, in MPa. Most friction data points should be found in the stippled area between I and M.

quality (heavily jointed and weathered), the failure criterion of Hoek & Brown (1980) may require smaller shear stress magnitude for slip to occur, than the friction criterion of Byerlee (1978) for rock samples.

Rupture, friction and depth: the Hoover Dam case

Analysis of dimensionless Mohr diagrams. Figure 8 summarizes the results of Mohr diagram analyses at Hoover Dam. The fault slip data are the same as in Table 1. However, 19% of faults, with individual angles (s, τ) larger than 20°, have been eliminated before plotting the Mohr diagrams.

The procedure for plotting Mohr diagrams consists of calculating for each fault the magnitudes of normal stress and shear stress (Fig. 2), as a function of the stress tensor previously determined (Table 1, Fig. 3). Because this tensor is not the actual stress tensor **T** but a reduced tensor $k\mathbf{T} + l\mathbf{I}$, where k and l are unknown and may be chosen arbitrarily, the normal stress magnitude calculated depends on k and l, and the shear stress magnitude depends on k (Fig. 2). As a consequence, the scale factor

Table 2. Results of Mohr diagram analyses

Fault set	Number of points	Ratio Φ	Ratio Ψ	Angle ω	Slope $\mu = tg\omega$	Angle 2θ	Mohr diagram in Fig. 8
n_1	88	0.21	0.05	25	0.47	60	Aa
n_2	98	0.22	0.08	24	0.45	63	Ac
n_3	118	0.18	0.04	28	0.53	61	Ab
n_4	66	0.30	0.08	29	0.55	54	Ad
Average	93	0.23	0.06	27	0.51	60	Ae
d_1	100	0.12	0.32	12	0.21	64	Ba
d_2	89	0.27	0.17	22	0.40	63	Bc
d_3	153	0.18	0.10	23	0.42	64	Bb
d_4	107	0.33	0.38	11	0.19	58	Bd
Average	112	0.23	0.24	17	0.31	62	Be

$n_1 - n_4$, predominantly normal fault sets and $d_1 - d_4$, predominantly strike-slip fault sets (as in Table 1). All values refer to Mohr diagrams of Fig. 8. All angles in degrees. Φ, Ψ, ω and 2θ defined in text and in diagrams (e) of Fig. 8. Fault slip data sets n_2, d_2 and n_4, d_4, shown in Fig. 3 (see also Table 1).

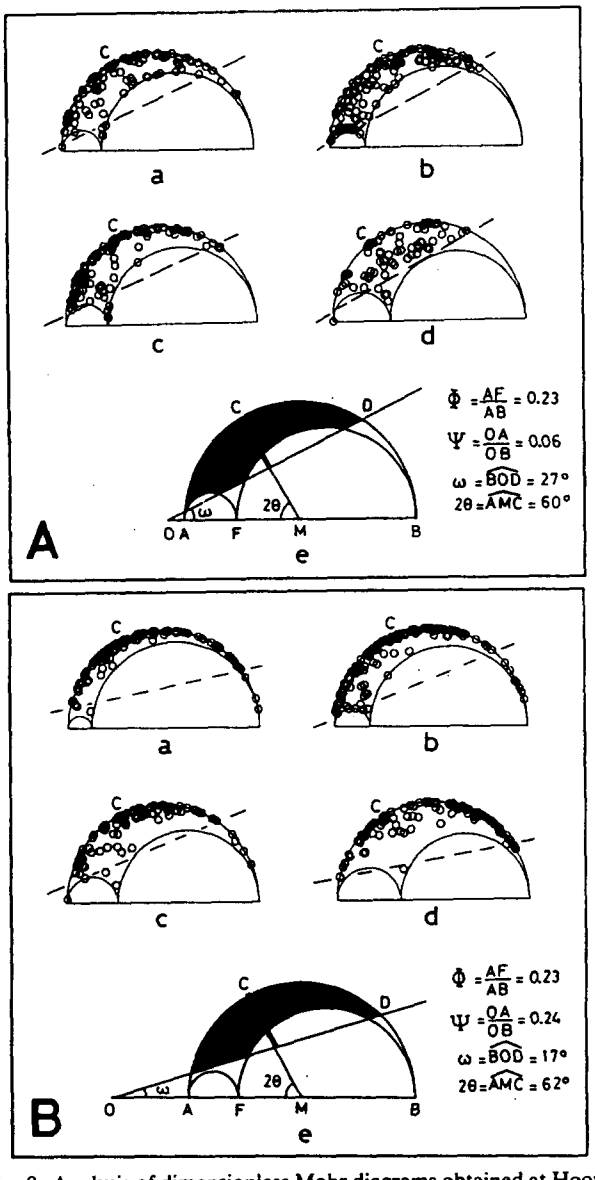

Fig. 8. Analysis of dimensionless Mohr diagrams obtained at Hoover Dam. A (upper half of figure): predominantly normal faulting mode. B (lower half): predominantly strike-slip faulting mode. Diagrams (a), (b), (c) and (d) refer to tectonic substages defined in Table 1; numerical results and reference numbers are listed in Table 2. Individual fault slip data are plotted as small open circles. Lower boundary of the mass of representative points is shown as a pecked line. C, points corresponding to conjugate faults. Diagrams (e) depict geometrical significance of parameters given in Table 2 and discussed in text (ratios Φ and Ψ, angles ω and 2θ), with average values for each faulting mode.

of the Mohr diagrams is unknown (k) and the position of the origin of abscissae is unknown too (l).

The results obtained for the four tectonic substages are given separately for normal and strike-slip dominated faulting modes (Fig. 8, Table 2). Individual diagrams display rather consistent patterns for each mode, so that results are reliably summarized in diagrams (e) of Fig. 8, and by average values in Table 2. Despite data dispersion, a reasonable approximation for the minimum friction line (less than 6% of points remain below the line) provides angles, ω, of 27° for normal faulting (Fig. 8A), and 17° for strike-slip faulting (Fig. 8B). These angles, ω, correspond to slopes, μ, of 0.5 and 0.3 (respectively). All values found in the dimensionless Mohr diagrams of Fig. 8 are in good agreement with those independently given by initial friction data, as comparison with Fig. 7 (b) shows.

These distributions of points for inherited faults in the Mohr diagram constrain the ratio Ψ, which has low values (0.06) for normal faulting and higher values (0.24) for strike-slip faulting (Fig. 8, Table 2). One may observe that although the Mohr diagrams have been plotted without scale and abscissa origin, determination of the Ψ ratio using slip data from inherited faults allows determination of the abscissa origin in Fig. 8, because the friction lines intersect the origin.

The only remaining unknown is the scale factor (referred to as k in Fig. 2). This factor k will be determined using the relationship between conjugate fault properties and failure envelope (Fig. 6a). Neoformed conjugate faults have been identified in fault slip data sets based on geometrical analysis (Fig. 4). They correspond to point concentrations on the largest Mohr circle (Fig. 8). The corresponding angle 2θ is read either from stereodiagrams (Fig. 4) or in Mohr diagrams (Fig. 8); it averages 61° for normal as well as strike-slip fault systems.

Rock mechanics analyses made at the Hoover Dam site indicate that the uniaxial compressional strength, σ_c, of the most common rocks (including ash-flow tuff units from which most of the structural data were collected) averages 40 MPa (U.S. Bureau of Reclamation 1950). This value is in agreement with those published in the

literature for similar rock types (Handin 1966, Vutukuri *et al.* 1974, Lama & Vutukuri 1978) for intact samples. With this value, the empirical criterion of Hoek & Brown (1980) for volcanic rocks has been adopted with the appropriate parameters ('good quality' jointed rock mass: empirical constants in Hoek & Bray 1981). Consistency with available information on tensile strength of intact rock has been checked. One thus obtains the failure envelope (as in Fig. 7). Because most fractures developed very early in the history of the rock mass, no variation of the failure envelope with time was assumed.

With the Mohr diagram patterns shown in Fig. 8, and the position of the origin already determined using friction data (ratio Ψ), the best fit between this failure envelope and the largest Mohr circle is obtained for stress magnitudes σ_3 and σ_1 that, respectively, average 0.5 and 7–9 MPa for the normal faulting mode, and 6–8 and 25–33 MPa for the strike-slip faulting mode. Because the ratio Ψ has been computed in the first step as an element of the reduced stress tensor, the magnitude of intermediate stress σ_2 is thus fixed (2–2.5 and 10–14 MPa, for normal and strike-slip modes, respectively).

Paleodepth and lithostatic load. An additional constraint given by geological reasoning about the depth of overburden and the corresponding lithostatic load should now be discussed. According to site studies and reports of the U.S. Bureau of Reclamation (1950), an erosional surface with gullies has been observed about 200 m above the sites of data collection; furthermore, an older erosional surface covered with basalts (Fortification Hill) is found about 800 m above these sites. The major faulting events occurred before deep Plio-Quaternary downcutting by the Colorado river drainage system. A value of between 200 and 800 m is a reasonable estimate for the depth of the site during most of the tectonic events considered. Shallower depths are likely for earlier (syn-depositional) or younger (post-erosional) tectonism. A more refined determination of paleostress magnitudes through time should take such changes into account. In this paper, the magnitudes calculated correspond to an average situation for the four tectonic substages.

With these depths of 200 and 800 m and an average rock density of 2.6–2.7 g cm^{-3}, one obtains lithostatic pressures of 5 and 20 MPa respectively. These values are direct estimates of the maximum principal stress, σ_1, (for normal faulting mode) or intermediate principal stress, σ_2, (for strike-slip faulting mode). The determinations discussed above and based on rupture-friction analyses solely have yielded values of 7–9 MPa for σ_1 in the normal faulting mode, and 10.5–14 MPa for σ_2 in the strike-slip faulting mode. These estimates are fairly compatible with the range of 5–20 MPa now obtained based on independent lithostatic pressure determination.

Table 3 summarizes the relationship between the three principal stress magnitudes, the vertical stress, σ_v, and the two parameters Φ and Ψ defined earlier.

Table 3. Determination of the three principal stresses as functions of the vertical load, σ_v, using Φ and Ψ ratios defined in text

	σ_1 vertical (predominantly normal faults)	σ_2 vertical (predominantly strike-slip faults)	σ_3 vertical (predominantly reverse faults)
$\sigma_1 =$	σ_v	$\dfrac{\sigma_v}{\Phi + \Psi - \Phi\Psi}$	$\dfrac{\sigma_v}{\Psi}$
$\sigma_2 =$	$\sigma_v (\Phi + \Psi - \Phi\Psi)$	σ_v	$\dfrac{\sigma_v}{\Psi (\Phi + \Psi - \Phi\Psi)}$
$\sigma_3 =$	$\sigma_v \Psi$	$\dfrac{\sigma_v \Psi}{\Phi + \Psi - \Phi\Psi}$	σ_v

Φ, ratio between principal stress differences computed with determination of the reduced stress tensor as in Fig. 3 and Table 1; Ψ, ratio between extreme principal stresses computed using friction data and Mohr diagrams as in Fig. 8 and Table 2.

Stress magnitudes. Taking all these results into account, as well as the additional constraint that σ_1 in the normal faulting mode should be equal to σ_2 in the strike-slip faulting mode (these modes have alternated very rapidly, so that no significant change in vertical stress in dry conditions may have occurred), reasonable average magnitudes of principal stresses σ_1, σ_2 and σ_3 at Hoover Dam are obtained: 10, 3 and 0.6 MPa, respectively, in the normal faulting mode, and 25, 10 and 6 MPa, respectively, in the strike-slip faulting mode. These low values suggest that depth during most faulting was closer to the shallowest case (200 m) than to the deepest one (800 m): a vertical stress of 10 MPa corresponds to a depth of about 400 m in dry conditions. Figure 9 illustrates the geometrical relationships between the unique rupture curve, the friction laws and the two sets of Mohr circles, for the two main faulting modes present at Hoover dam. For each of the faulting modes, the similarity of Mohr diagrams shown in Figs. 8 (A) & (B) suggests that there is no major difference in paleostress magnitudes between different substages. However, this similarity may also be accounted for by the lack of resolution, and somewhat different depth and stress conditions may have prevailed during the two main tectonic events: the average situation is described.

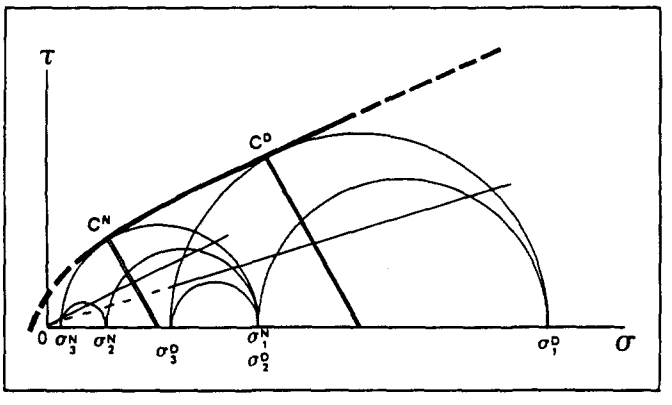

Fig. 9. Relationship between stress magnitude determinations made at Hoover Dam locality for predominantly normal faulting mode (symbol N) and predominantly strike-slip faulting mode (symbol D). Mohr diagram (σ normal stress, τ shear stress). Principal stresses σ_1, σ_2 and σ_3, shown for modes N and D. Failure envelope shown as thick line, with C referring to conjugate fault systems. Friction lines shown as thin lines. Numerical results discussed in the text.

All determinations have been made implicitly assuming that fault tectonics occurred in a dry rock mass, that is, in the zero pore pressure case. Considering the hydrostatic pore pressure case, that is rock saturated with water, implies that effective stress magnitudes are computed by removing the hydrostatic head. This results in dramatically diminishing the stress levels required for failure and friction to occur. However, the least principal stress should remain larger than the pore pressure; otherwise, the pore pressure would hydro-fracture the rock resulting in the opening of tension cracks instead of sliding on neoformed and inherited faults. Tension cracks are more numerous at Hoover Dam in the upper layers than at the level of sites where fault slip data have been collected.

As a consequence of taking into account variable pore pressure, note that in some tectonic stress conditions the existence and variations in level of water table may control the effective stress and hence the development and type of brittle deformation.

Discussion: a method of determining paleostress magnitudes

Previous analyses. Earlier attempts at estimating paleostress magnitudes using fault slip analysis (principally for strike-slip tectonic mode) have been made in various geological settings. Most determinations are based on fitting the largest Mohr circle with failure envelopes obtained from the literature (Petit 1976), or from rock mechanics experiments on samples collected at the same site as fault slip data (Bergerat *et al.* 1982, 1985). Byerlee's friction laws have been applied to slip on large normal faults in north central Nevada by Zoback & Zoback (1980), who also took into account the effects of hydrostatic head by considering as limits the hydrostatic pore pressure and zero pore pressure cases. All authors have included the determination of vertical stress based on depth and average rock density to fix one of the principal stresses. Provided that sites at different depths are available for a single tectonic event and that assumptions on variations of horizontal stress with depth are made, additional constraints are obtained (Rispoli 1981, Rispoli & Vasseur 1983).

The method. The method proposed here is applicable to a single site and combines reasoning on rupture, friction and depth data (Fig. 6). To use rupture data, it is necessary; (1) to identify conjugate fault systems and (2) to determine the shape of the rupture curve, as shown in Figs. 6 (a) and 7 (a). Conjugate fault systems are easily found in the field (Fig. 4), even in sites where most faults are reactivated planes of weakness (Fig. 3). The failure envelope is determined either from rock mechanics experiments on samples from the studied site, or from the rock mechanics literature. Compressive and tensile strengths are generally known; using their values, I consider the empirical equation of Hoek & Brown (1980) as a realistic approach.

Particular attention should be paid to the choice of rock mass quality (which may differ widely from rock sample quality), because it drastically influences the slope of the failure envelope (Fig. 7a) and consequently controls the size of the main Mohr circle. This major constraint will be discussed later. The relationship between stress magnitudes σ_1 and σ_3 when failure occurs may be obtained by analytical derivation from Hoek and Brown's equation. One may also check the fit between the Mohr circle and the failure envelope by simple geometrical means. In both cases, the relationship between the slope of the failure envelope at the point of tangency and the dihedral angle, 2θ, between conjugate faults imposes an additional constraint (Fig. 6a), thus enabling one to check consistency.

To use friction data, it is necessary to observe a large variety of oblique inherited faults that correspond in a Mohr diagram to points between the three Mohr circles. The slope of the linear initial friction curve is obtained by direct observation of the point distribution, as in Fig. 8. Estimates of the angle ω and the related friction coefficient, μ, obtained in dimensionless Mohr diagrams at Hoover Dam (Fig. 8) are compatible with usual values (Byerlee 1978) (Fig. 7b). In any case, the fit between point distribution and friction line in a dimensionless Mohr diagram fixes the value of the ratio Ψ (Fig. 6b).

The two independent relationships derived from rupture and friction data enable one to determine the magnitudes of σ_1 and σ_3. The technique consists of fitting the rupture curve shown in Fig. 6 (a) and the friction line of Fig. 6 (b) with a single $\sigma_1 - \sigma_3$ Mohr circle, and checking agreement with the dihedral angle, 2θ, of the conjugate faults (Fig. 6a). This may be done by geometrical or numerical means. The magnitude of the intermediate stress, σ_2, is thus fixed as a function of the magnitudes of σ_1 and σ_3, because the ratio Φ has been determined earlier. The relationships between principal stress magnitudes, Φ ratio, Ψ ratio, and vertical load σ_v are given in Table 3. Note that the failure criterion of Fig. 6 (a) is not involved in these relationships. In the case of the Hoover Dam site, determination of the vertical stress, σ_v, from depth and rock density estimates has been used simply in order to check the general consistency of results.

Where fracture or friction data are poorly constrained, the determination of the vertical stress becomes a critical step in the process (Fig. 6 c). For instance, the analysis of friction data and the depth reconstruction (Figs. 6b & c) allows hypotheses on the shape of the actual failure envelope (and hence on rock mass quality) according to Hoek and Brown's empirical parameters (Figs. 6a and 7a).

Rock mass quality and pore pressure. At the same depth and for a similar fault tectonic mode (dominantly strike-slip, Fig. 8b), the average stress magnitudes obtained in the Hoover Dam site (this paper) are surprisingly low compared with the results of earlier determinations in southern Germany (Bergerat *et al.* 1982, 1985). Computed deviatoric stresses in dry conditions range from 10 to 40 MPa (Hoover Dam) and from 50 to 130

MPa (Germany). Most of the differences cannot be accounted for by contrasts in lithology and rock sample strengths.

Variations in tectonic context certainly play a role (strike-slip faulting is associated with normal faulting at Hoover Dam and with reverse faulting in southern Germany, so that a higher tectonic stress level is to be expected in the latter case). This contrast in tectonic environment (extensional Basin and Range tectonism for Hoover Dam, peri-Alpine compressional tectonism in Southern Germany) partly explains differences in paleostress levels required for strike-slip faulting to occur.

Another critical factor is the difference between the failure envelopes. These curves have been determined for intact rock samples in the case of southern Germany, and for a rock mass of a certain quality (according to parameters tabulated by Hoek & Bray 1981) in the case of the Hoover Dam. As Fig. 7(a) suggests, adopting in the case of the Hoover Dam the failure envelope for intact samples instead of 'good quality' mass, would lead to determination of larger magnitudes (the failure envelope is higher). To summarize, a major source of apparent disagreement between these estimates of stress amplitudes in strike-slip tectonic environment is the contrast in rock mass properties. These properties have been considered similar to rock sample properties in the case of southern Germany. In contrast, because the Hoover Dam rock masses have obviously been jointed and fractured prior to the faulting events considered, their strength is considered smaller than the strength of small intact rock pieces.

Note, incidentally, that differences between rock properties at the present and at the time of faulting should be considered where faulting predates complete lithification; other phenomena, such as weathering, should also be taken into account.

Finally, a crucial factor in stress magnitude determination is the existence of pore pressure. Because all determinations have been discussed in the absence of hydrostatic head, the values calculated should be considered as maximum values of effective stress. Actual magnitudes of effective stresses obviously lie between the values computed in the zero and hydrostatic pore pressure cases. A better approximation would require determination of the nature and amount of rock porosity in order to compute the actual pore pressure, and hence the actual effective stress.

Acknowledgements—Earlier discussions with M.-L. and M. Zoback were useful. J. Thompson and P. Hancock helpfully read the text. Research has been supported by the French C.N.R.S.

REFERENCES

Anderson, E. M. 1942. *The Dynamics of Faulting* (2nd edn). Oliver & Boyd, Edinburgh.

Anderson, R. E. 1969. Notes on the geology and paleohydrology of the Boulder City pluton, southern Nevada. *Prof. Pap. U.S. geol. Surv.* **650-B**, B35–B40.

Anderson, R. E. 1971. Thin-skinned distension in Tertiary rocks of southeastern Nevada. *Bull. geol. Soc. Am.* **82**, 43–58.

Anderson, R. E. 1973. Large magnitude late Tertiary strike-slip faulting north of Lake Mead, Nevada. *Prof. Pap. U.S. geol. Surv.* **794**.

Angelier, J. 1975. Sur l'analyse de mesures recueillies dans des sites faillés: L'utilité d'une confrontation entre les méthodes dynamiques et cinèmatiques. *C.r. Acad. Sci., Paris* **D281**, 1805–1808.

Angelier, J. 1979. Determination of the mean principal stresses for a given fault population. *Tectonophysics* **56**, T17–T26.

Angelier, J. 1984. Tectonic analysis of fault slip data sets. *J. geophys. Res.* **89**, 5953–5848.

Angelier, J., Colletta, B. & Anderson, R. E. 1985. Neogene paleostress changes in the Basin and Range: a case study at Hoover Dam, Nevada-Arizona. *Bull. geol. Soc. Am.* **96**, 347–361.

Angelier, J., Lybéris, N., Le Pichon, X., Barrier, E. & Huchon, P. 1982a. The tectonic development of the Hellenic arc and the Sea of Crete: a synthesis. *Tectonophysics* **86**, 159–196.

Angelier, J. & Mechler, P. 1977. Sur une méthode graphique de recherche des contraintes principles également utilisable en tectonique et en séismologie: la méthode des dièdres droits. *Bull. Soc. géol. Fr.* **19**, 1309–1318.

Angelier, J., Tarantola, A., Valette, B. & Manoussis, S. 1982b. Inversion of field data in fault tectonics to obtain the regional stress. I. Single phase fault populations: a new method of computing the stress tensor. *Geophys. J. R. astr. Soc.* **69**, 607–621.

Armijo, R. & Cisternas, A. 1978. Un problème inverse en microtectonique cassante. *C. r. Acad. Sci., Paris* **D287**, 595–598.

Barrier, E. & Angelier, J. 1986. Active collision in eastern Taiwan: the coastal Range. *Tectonophysics* **125**, 39–72.

Bergerat, F. 1987. Stress fields in the European platform at the time of Africa–Eurasia collision. *Tectonics* **6**, 99–132.

Bergerat, F., Bergues, J. & Geyssant, J. 1982. Estimation des contraintes liées à la formation de décrochements dans la plateforme carbonatée de l'Allemagne du Sud. *C.r. Acad. Sci., Paris* **295**, 1155–1160.

Bergerat, F., Bergues, J. & Geyssant, J. 1985. Estimation des paléocontraintes liées à la formation de décrochements dans la plateforme d'Europe du Nord. *Geol. Rdsch.* **74**, 311–320.

Bott, M. H. P. 1959. The mechanisms of oblique slip faulting. *Geol. Mag.* **96**, 109–117.

Byerlee, J. D. 1978. Friction of rocks. *Pure & appl. Geophys.* **116**, 615–626.

Carey, E. & Brunier, B. 1974. Analyse théorique et numérique d'un modèle mécanique élémentaire appliqué à l'étude d'une population de failles. *C.r. Acad. Sci., Paris* **D179**, 891–894.

Etchecopar, A., Vasseur, G. & Daignières, M. 1981. An inverse problem in microtectonics for the determination of stress tensors from fault striation analysis. *J. Struct. Geol.* **3**, 51–65.

Gauthier, B. & Angelier, J. 1985. Fault tectonics and deformation: a method of quantification using field data. *Earth Planet. Sci. Lett.* **74**, 137–148.

Gephart, J. W. & Forsyth, D. W. 1984. An improved for determining the regional stress tensor using earthquake focal mechanism data: an application to the San Fernando earthquake sequence. *J. geophys. Res.* **B89**, 9305–9320.

Hancock, P. L. 1985. Brittle microtectonics: principles and practice. *J. Struct. Geol.* **7**, 437–457.

Handin, J. 1966. Strength and ductility. In: *Handbook of Physical Constants* (edited by Clark, S. P.). Geol. Soc. Am., New York, 223–289.

Hoek, E. & Bray, J. W. 1981. *Rock Slope Engineering* (5th edn). The Institution of Mining and Metallurgy, London.

Hoek, E. & Brown, E. T. 1980. *Underground Excavations in Rock.* The Institution of Mining and Metallurgy, London.

Jaeger, J. C. 1969. *Elasticity, Fracture and Flow* (3rd edn). Chapman & Hall, London.

Jaeger, J. C. & Cook, N. G. W. 1969. *Fundamentals of Rock Mechanics.* Methuen, London.

Lama, R. D. & Vutukuri, V. S. 1978. *Handbook on Mechanical Properties of Rocks. Testing Techniques and Results.* Vol. II. *Series on Rock and Soil Mechanics* **3**. Trans. Tech Publications.

Lisle, R. J. 1979. The representation and calculation of the deviatoric component of the geological stress tensor. *J. Struct. Geol.* **1**, 317–321.

Lisle, R. J. 1987. Principal stress orientations from faults: an additional constraint. *Ann. Tectonicae* **1**, 155–158.

Longwell, C. R. 1936. Geology of the Boulder Reservoir floor, Arizona, Nevada. *Bull. geol. Soc. Am.* **47**, 1393–1476.

Mattauer, M. 1973. *Les Déformations des Matériaux de l'Ecorce Terrestre.* Hermann, Paris.

Michael, A. 1984. Determination of stress from slip data: faults and folds. *J. geophys. Res.* **B89**, 11,517–11,526.

Petit, J. P. 1976. La zone de décrochements du Tizi N'Test (Maroc) et son fonctionnement depuis le Carbonifère. Unpublished thèse 3ème cycle, Université de Montpellier.

Rispoli, R. 1981. Microtectonique et champ de contraintes dans les calcaires fins du Languedoc. Exemple des Matelles et du cirque de Navacelles. Unpublished thèse 3ème cycle, Université de Montpellier.

Rispoli, R. & Vasseur, G. 1983. Variation with depth of the stress tensor anisotropy inferred from microfault analysis. *Tectonophysics* **93**, 169–184.

U.S. Bureau of Reclamation. 1950. Geological investigations. In: *U.S. Bur. Recl., Boulder Canyon Project Final Reports*, part 3, (preparatory examinations), Bull. 1. Denver, Colorado.

Vutukuri, V. S., Lama, R. D. & Saluja, S. S. 1974. *Handbook on Mechanical Properties of Rocks. Testing Techniques and Results.* Vol. 1. *Series on Rock and Soil Mechanics*, 2. Trans. Tech Publications.

Wallace, R. E. 1951. Geometry of shearing stress and relation to faulting. *J. Geol.* **59**, 118–130.

Zoback, M. L. Anderson, R. E. & Thompson, G. A. 1981. Cainozoic evolution of the state of stress and style of tectonism of the Basin and Range province of the western United States. In: *Extensional Tectonics Associated With Convergent Plate Boundaries* (edited by Vine, F. J. & Smith, A. G.). *Proc. R. Soc. Lond.*, 189–216.

Zoback, M. L. & Zoback, M. D. 1980. Faulting patterns in North-Central Nevada and strength of the crust. *J. geophys. Res.* **B85**, 275–284.